Present-day and Long-term Uplift Across the Western Transverse Ranges of Southern California

K.M. Johnson[1], W.C. Hammond[2], R.J. Burgette[3], S.T. Marshall[4], and C.C. Sorlien[5]

1. Department of Earth and Atmospheric Sciences, Indiana University, Bloomington, IN
2. Nevada Geodetic Laboratory, Nevada Bureau of Mines and Geology, University of Nevada, Reno, Reno, NV
3. Department of Geological Sciences, New Mexico State University, Las Cruces, NM
4. Department of Geological and Environmental Sciences, Appalachian State University, Boone, NC
5. Earth Research Institute, University of California, Santa Barbara, CA

Key Points

1. We invert geodetic and geologic data for slip rate and coupling on faults in the Western Transverse Ranges (WTR) using a kinematic model.
2. Much of the vertical velocity field in the WTR can be attributed to the interseismic signal of strain accumulation on reverse faults.
3. Sum of fault dip-slip rates across the WTR decreases from 10.5-14.6 mm/yr onshore to 5-6.2 mm/yr across the western Santa Barbara Channel.

1. Abstract

It has been known for decades that the present-day shortening rates across the Western Transverse Ranges (WTR) in southern California are rapid, reaching 10-15 mm/yr near the heavily populated Los Angeles area. However, only recently have geodetic measurements of vertical motion in the WTR been sufficiently dense to resolve a tectonic vertical signal. In this study, we show that much of the geodetically-derived vertical velocity field in the WTR can be attributed to the interseismic signal of strain accumulation on reverse faults. We invert geodetic and geologic data for slip rate and interseismic coupling on faults using a kinematic

model consisting of faults embedded in an elastic crust over an inviscid mantle. This method allows us to infer the permanent, long-term component of vertical motions from recoverable, short term motions. We infer that much of the geodetically observed 3-4 mm/yr of differential vertical motion across the WTR, involving subsidence along the Santa Barbara coastline and uplift of the Santa Ynez Range, can be attributed to recoverable elastic deformation associated with interseismic locking on faults dipping under the WTR. The sum of dip-slip rates across the WTR decreases from 10.5-14.6 mm/yr on the east side near Ventura, California to 5-6.2 mm/yr across the western side of the Santa Barbara Channel. The total moment accumulation rate in both the Santa Barbara Channel and the combined San Fernando Valley-LA Basin regions is equivalent to about two M_w=7 earthquakes every 100 years.

2. Introduction

There is a growing interest in earthquake hazards associated with the active fold-and-thrust belt of the Western Transverse Ranges (Figure 1) in southern California near the heavily populated greater Los Angeles area (Hubbard et al., 2014; Marshall et al., 2017; McAuliffe et al., 2015; Rockwell et al., 2016). GPS-derived horizontal velocities across this belt indicate as much as ~10 mm/yr of N-S shortening at the longitude of Ventura, California (Figure 2a) with decreased shortening to the west. Kinematic models of the present-day velocity field prepared for the Uniform California Earthquake Rupture Forecast Version 3 (Field et al., 2014) and mechanical deformation models for the region (Marshall et al., 2013; Marshall et al., 2017) indicate summed reverse-slip rates across the WTR and Santa Barbara Channel exceed 10 mm/yr. These models, as well as Hubbard et al. (2014), suggest that 4-7 mm/yr of reverse slip may occur on the Ventura-Pitas Point fault system. This system forms the northern boundary of the Ventura Basin extending from onshore near the San Fernando Basin to offshore Santa Barbara Channel at least 20 km west of the city of Santa Barbara (Figure 1a). McAuliffe et al. (2015) and Hubbard et al. (2014) suggested the possibility of past and future large (M_w = 7.5-8) earthquakes on this fault system based on paleoseismic and structural investigations.

The Western Transverse Ranges (WTR) comprise a series of complex, largely E-W trending oblique reverse faults and folds west of the "Big Bend" of the San Andreas fault. The three-dimensional geometry of the faults in the region is illustrated in Figure 1b. This geometry is a compilation from the Southern California Earthquake Center (SCEC) Community Fault Model (Plesch et al., 2007), the UCERF3 fault model (Field et al., 2014), and Sorlien and Nicholson (2015). The shallow geology is shown in cross section A-A' in Figure 1c, based on cross sections by Namson and Davis (1988) (see also thomasldavisgeologist.com). The trace of model faults within the vicinity of profile A-A' are shown on the geologic cross section.

Geologic and paleomagnetic data indicate the WTR have rotated clockwise into the current configuration since early Miocene, ca. 20 Ma, in response to the transition from subduction to transform faulting along the San Andreas Fault (Hornafius et al., 1986; Kamerling and Luyendyk, 1985; Nicholson et al., 1994). Seismic and geodetic data indicate that this rotation continues to this day (Jackson and Molnar, 1990). The current fold-thrust belt configuration has been active since contraction across the WTR initiated between 5.3 and 4.5 Ma (Clark et al., 1991; Schneider et al., 1996; Sorlien et al., 2000). Comparisons of structural restoration of seismically-imaged deformed horizons of age 1-6 Ma (Gratier et al., 1999; Sorlien et al., 2000) with restorations of the younger 250-500 ka Saugus Formation (Huftile and Yeats, 1995) indicate shortening rates have increased across the eastern Ventura Basin from 1-3 mm/yr (pre-1 Ma) to at least 10-14 mm/yr (post-1 Ma). The later rates are generally consistent with present-day rates of shortening determined with geodetic data (e.g., Donnellan et al. (1993); Figure 2). The extraordinarily thick Ventura Basin sedimentary section is estimated to be 14-17 km thick (Luyendyk and Hornafius, 1987). The basin subsidence rate since ~1 Ma is 2-3 mm/yr (Yeats, 1983).

Most previous kinematic models constrained by geodetic data in the region used 2D fault geometry and sparse geodetic observations (Donnellan et al., 1993; Hager et al., 1999) or simplified 3D fault geometry using block model formulations (Johnson, 2013;

McCaffrey, 2005; Meade and Hager, 2005b). The UCERF3 deformation models mentioned above used more detailed 3D fault geometry than previously published studies, but the UCERF models did not attempt to model all of the regional faults. Marshall et al. (2013) and Marshall et al. (2017) developed boundary element models of all of the currently known active faults in order to estimate slip rates and compare with geodetic data in the region. Marshall et al. (2017) showed that boundary element models produce 3-6 mm/yr of slip on the onshore Ventura fault and predict uplift of 1-2 mm/yr across the Santa Ynez Mountain Anticlinorium (Figure 1c).

Hammond et al. (2018) constructed a vertical geodetic deformation field for the WTR by combing observations from four techniques including GPS, InSAR, leveling, and tide gauges (Figure 2b). This new dense vertical field warrants the reexamination of present-day deformation across the WTR in combination with the existing horizontal GPS velocity field used to constrain kinematic models in previous studies. Authors have shown previously that the present-day vertical deformation field is an important constraint on deciphering the distribution of deformation across faults in convergent settings (Beavan et al., 2010; Ching et al., 2011; Huang et al., 2010; Johnson et al., 2005). In particular, the vertical interseismic signal provides constraint on the down-dip extent of interseismic coupling on dip-slip faults (e.g. Marshall et al., 2017). Here, we combine the new geodetic vertical field with other observations to infer the distribution of deformation across the WTR.

All of the data used in this study have been published previously (Figure 2). The horizontal GPS-derived velocity field is the SCEC Crustal Motion Map 4, (CMM4; Shen et al., 2011). The velocity field is shown relative to Santa Rosa Island. The vertical geodetic velocity field is from Hammond et al. (2018), as discussed previously. The "long-term", geologic vertical rates are taken from the SCEC geologic vertical motion map (Niemi et al., 2008) which is a compilation of various inferences of vertical motion derived from marine terraces, incised river terraces, thermochronologic ages, and stratigraphic surfaces. We augment the Niemi et al. (2008) data set with the offshore ~1 Ma stratigraphic surface in the central Santa Barbara

Basin (Sorlien and Nicholson, 2015; Sorlien et al., 2016; Yeats, 1981). While all of these datasets have been published previously, we present here the first model that integrates these data to constrain a model of long and short-term horizontal and vertical motions in the region.

In this paper, we combine the geologic measurements of uplift rate with geodetic measurements of vertical and horizontal motion into a single model for recent deformation across the Western Transverse Range fold and thrust belt. In particular, we are interested in examining to what extent the observed pattern in the geodetic vertical field is a tectonic signal due to slip on active faults and associated crustal flexure. For example, is the broad upward arching across much of the WTR (Figure 2b) a signature of deep aseismic slip on reverse faults underlying the ranges? Is this interseismic vertical signal consistent with observed shortening rates inferred from geodesy and longer-term uplift rates inferred from geology? How much of the observed interseismic uplift will eventually be expressed in the long-term uplift and topographic growth of the Western Transverse Ranges? To address these questions, we need an appropriate model that will allow us to make predictions of interseismic vertical and horizontal motions as well as longer-term vertical motions. This model is discussed in the next section.

3. Model and Inverse Method

For this study, we adopt an elastic plate based kinematic modeling approach that is different from previous kinematic models of interseismic deformation. Elastic halfspace block models are the most commonly used kinematic method to estimate fault slip rates using geodetic data. However, such elastic block models traditionally assume no long-term vertical motion (e.g., McCaffrey (2005); Meade and Hager (2005a)) and are therefore not suitable for this study. Johnson and Fukuda (2010) developed a viscoelastic block model that is able to capture long-term vertical motions. In that model, fault-bounded blocks are constructed in an elastic plate overlying a viscoelastic halfspace and steady-state and interseismic vertical motions due to dip-slip faulting are explicitly

modeled. Huang et al. (2010) used that model to reconcile present-day vertical and horizontal motions with Holocene uplift rates in eastern Taiwan. However, the geologic setting in our study of the WTR is not ideal for block models. There are many non-planar, closely-spaced, and discontinuous fault strands in the region that do not clearly delineate crustal blocks. Other dislocation-based kinematic modeling approaches avoid the construction of fault-bounded blocks. For example, Zeng and Shen (2014) and Smith and Sandwell (2006) devised kinematic interseismic deformation models in which an elastic halfspace or elastic plate is populated with faults and deformation is generated by imposing slip on the faults. Our approach here is similar in this sense to the non-block approach of Smith and Sandwell (2006) and Zeng and Shen (2014).

3.1 Forward model

The geometry of the model is illustrated in Figure 3a. We populate an elastic plate overlying an inviscid substrate with three-dimensional fault surfaces. We generate the model velocity field by imposing slip on the faults. As in traditional block modeling, the total interseismic velocity field is the sum of two components: a long-term, steady-state velocity field in which the faults slide at their long-term fault slip rate, and an interseismic contribution due to coupling on faults. The long-term field is constructed by imposing forward slip at a steady rate on all the faults using the solution for faulting in an elastic plate over an inviscid halfspace, as in Huang et al. (2010). The inviscid response is obtained from the solution for fully relaxed viscous flow in a halfspace below the elastic plate. The plate is subjected to gravitational restoring forces, so the long-term vertical motion is compensated isostatically. For simplicity, we assume spatially uniform slip rate on each fault segment. For the interseismic period, we assume the viscoelastic relaxation time of the mantle is long compared to the repeat time of earthquakes. In this case, interseismic flow in the viscoelastic mantle is steady with time throughout the interseismic period and the interseismic contribution to deformation can be constructed with backslip on a dislocation in an elastic halfspace (e.g., Savage and Prescott, 1978) . Our approach here is similar to that of Huang et al. (2010) and Johnson and Fukuda (2010), except the plate model in those studies required the construction of fault-bounded blocks, which is not required with the present method.

To capture the far-field relative plate motion across the fault system, the San Andreas fault is extended to effectively infinite distance to the north and south of the model domain and a composite "Borderland" fault is extended to the south of the model domain. Slip is imposed on the fault extensions at the rates shown in Figure 3a. Backslip on faults is imposed between a specified upper and lower locking depth at the long-term slip rate of the fault. Thus, faults creep interseismically above the upper locking depth to the surface and below the lower locking depth down to the bottom of the elastic plate at the long-term fault slip rate. Backslip is imposed only on fault surfaces shown with color in Figure 3. Backslip is not imposed on the other fault surfaces because these sources are sufficiently far from the observations to not influence the predicted interseismic velocities. In this study we use an elastic plate thickness of 25 km, which corresponds with the average crustal thickness in the region (Tape et al., 2012).

Figure 3b illustrates the plate flexure model for the case of a 2D fault that is infinitely long in the strike direction. The purpose of this illustration is to provide insight into the horizontal and vertical deformation expected across an idealized reverse fault. The horizontal and vertical velocities, normalized by fault slip rate, are plotted for two different fault geometries: a straight fault that is locked from the surface to depth D, and a ramp-detachment-ramp fault geometry with the upper ramp locked interseismically. Horizontal long-term contraction is accommodated by nearly rigid-body motions on both sides of the fault. During the interseismic period, the horizontal contraction is spread out over a wider area because of interseismic locking on the fault. In both models shown in Figure 3b, the pattern of interseismic vertical motion is quite different from the long-term pattern. In particular, the interseismic coupling on the fault pushes the peak uplift, which occurs at the upper fault tip in the long-term, towards the position of the lower locked edge of the fault. Interseismic subsidence is predicted above much of the locked section.

3.2 Inverse Method

The parameters we seek to estimate in this inversion include fault slip rates for each segment, upper and lower locking depths for each segment, and data weights, as

discussed below. Let $\boldsymbol{s}$ be a vector of strike-slip rates, $\boldsymbol{r}$ be a vector of dip-slip rates, and $\boldsymbol{L}$ be a vector of upper and lower locking depths. We have three sets of observations as shown in Figure 2. Let $\boldsymbol{d}_i$, i=1,2,3, be three vectors of N_i observations. We assume the data errors are normally distributed with covariance matrix $\sigma_i^2\boldsymbol{\Sigma}_i$, i=1,2,3, where the $\boldsymbol{\Sigma}_i$ are formal data covariance matrices (diagonal in this study) and the σ_i^2 are unknown scale factors that determine the relative weighting of the i-th data set, and allow the data uncertainties to be inflated or reduced as needed to fit within uncertainties. To simplify notation below, we define the vectors $\boldsymbol{d} = [\boldsymbol{d}_1\ \boldsymbol{d}_2\ \boldsymbol{d}_3]$ and $\boldsymbol{\sigma} = [\boldsymbol{\sigma}_1\ \boldsymbol{\sigma}_2\ \boldsymbol{\sigma}_3]$. We seek the posterior probability distribution of unknown parameters, given data: $p(\boldsymbol{s},\boldsymbol{r},\boldsymbol{L},\boldsymbol{\sigma}|\boldsymbol{d})$. Bayes' theorem states that

$$p(\boldsymbol{s},\boldsymbol{r},\boldsymbol{L},\boldsymbol{\sigma}|\boldsymbol{d}) \propto p(\boldsymbol{d}|\boldsymbol{s},\boldsymbol{r},\boldsymbol{L},\boldsymbol{\sigma})p(\boldsymbol{s},\boldsymbol{r},\boldsymbol{L},\boldsymbol{\sigma}) \quad (1)$$

where $p(\boldsymbol{d}|\boldsymbol{s},\boldsymbol{r},\boldsymbol{L},\boldsymbol{\sigma})$ is likelihood and $p(\boldsymbol{s},\boldsymbol{r},\boldsymbol{L},\boldsymbol{\sigma})$ is the prior probability distribution on unknown parameters. Because we assume Gaussian data errors, the likelihood is

$$p(\boldsymbol{d}|\boldsymbol{s},\boldsymbol{r},\sigma) = \prod_{k=1}^{3}(2\pi\sigma_k^2)^{-N_k/2}|\Sigma_k|^{-\frac{1}{2}}$$
$$\times \exp\left[-\frac{1}{2\sigma_k^2}\left(\boldsymbol{d}_k - \widehat{\boldsymbol{d}}_{\boldsymbol{k}}(\boldsymbol{s},\boldsymbol{r},\boldsymbol{L})\right)^T\Sigma_k^{-1}\left(\boldsymbol{d}_k - \widehat{\boldsymbol{d}}_{\boldsymbol{k}}(\boldsymbol{s},\boldsymbol{r},\boldsymbol{L})\right)\right], \quad (2)$$

where $\widehat{\boldsymbol{d}}_{\boldsymbol{k}}$ is the model-predicted displacement for the k-th data set (e.g., Fukuda and Johnson, 2010) .

The priors are all uniform, bounded, uncorrelated distributions (boxcars), such that $p(\boldsymbol{s},\boldsymbol{r},\boldsymbol{L},\boldsymbol{\sigma}) = p(\boldsymbol{s})p(\boldsymbol{r})p(\boldsymbol{L})p(\boldsymbol{\sigma})$. The bounds for the prior on strike-slip and dip-slip rates, $p(\boldsymbol{s})$ and $p(\boldsymbol{r})$, are based loosely on the geologic slip rate model for UCERF3 (Field et al., 2014) for faults in our model that also exist in UCERF3 (the majority of our faults). The UCERF3 slip rate bounds (Dawson and Weldon, 2013) were assigned by expert opinion, based on published geologic slip rate estimates, where available, and the USGS Quaternary Fault and Fold Database slip rate categories. We take a conservative approach and constrain the sense of slip on each fault in our model based on this UCERF3 model, but increase the upper bounds of dip-slip and strike-slip motion. The conservative bounds

adopted for this study are tabulated in Table S1 and illustrated in Figure S1. We bound the lower locking depth between 20 km and the upper locking depth. We bound the upper locking depth between zero (the ground surface) and the lower locking depth. Finally, we apply positivity constraints to the data weights, $\boldsymbol{\sigma}$.

We adopt a Monte Carlo-Metropolis sampling algorithm to generate a discrete representation of the posterior distribution (e.g., Fukuda and Johnson, 2010).

4. Other causes of vertical surface motion

We should be mindful of known sources of vertical motion that are not considered in the plate deformation model described in the previous section. Loading of the crust by hydrological mass variations (e.g. ground water withdrawal) has been shown to generate significant vertical motions that could potentially mask vertical tectonic signals (e.g., Borsa et al. 2014; Fu et al. 2015; Argus et al., 2017). Of particular relevance to this study, Amos et al. (2014) showed that a zone of observed surface uplift of 1-3 mm/yr surrounding the San Joaquin Valley can be attributed to the elastic response of groundwater removal in the Valley. Amos et al. (2014) demonstrated the plausibility of this elastic response to a surface load with a 2D line load model. To examine the extent to which vertical motion shown in Figure 2b can be attributed to groundwater depletion in the San Joaquin Valley, we extend the Amos et al. (2014) model to 3D by considering a distribution of point normal surface loads on an elastic halfspace using the well-known Boussinesq solution (e.g, Timoshenko et al. (1951)). We integrate the Boussinesq point source to obtain the solution for a uniform load over a rectangular region. We discretize the San Joaquin Valley into rectangular cells of uniform load as shown in Figure 4. Following Amos et al. (2014), we assume a total rate of unloading of 3×10^{13} N/yr. We assign the spatial distribution of the surface load by assuming the load is proportional to the rate of subsidence observed in GPS data (Hammond et al., 2016). Figure 4 compares the observed vertical motions with the predictions of the surface loading model. The velocities are shown relative to the San Miguel and Santa Rosa islands (Figure 2a). Consistent with the Amos et al. (2014) model for the 2D case, the model predicts ~2

mm/yr of uplift rimming the edge of the San Joaquin Valley and decaying rapidly with distance from the valley. Figure 4c shows the residual vertical velocity field constructed by subtracting the predicted displacements from the observations. The model predictions account for much of the ~1-3 mm/yr of observed uplift along the Carrizo section of the San Andreas fault, but the model does not explain the broader uplift pattern extending south and west of the San Andreas fault. Figure 4d shows the observed and predicted vertical pattern along several N-S profiles across the Western Transverse Ranges. The monotonically decreasing uplift pattern from north to south predicted by the surface load model has a quite different spatial pattern from the arched uplift pattern seen in the data.

A potential source of vertical motion that we will ignore in our kinematic plate deformation model is non-steady mantle flow in response the earthquake cycle (e.g., Pollitz et al. (2001); DeVries et al. (2016)). Smith-Konter et al. (2014) and Howell et al. (2016) used a viscoelastic earthquake cycle model of interseismic deformation in southern California to show that mantle flow due to the repeated slip on faults over time can generate vertical surface motions of order 1-2 mm/yr. In Figure 5a-b, we show the predicted vertical motion due to transient mantle flow from the viscoelastic earthquake cycle model of Johnson (2013). This model assumes faulting in a 25-km thick elastic plate overlying a 25 km-thick lower crust/upper mantle with viscosity 5×10^{20} Pa s overlying a mantle with viscosity 5×10^{18} Pa s. Figure 5a shows the contribution from all strike-slip faults and Figure 5b shows the contribution from only the San Andreas and San Jacinto faults. Here we are showing only transient vertical motions; motion due to steady long-term slip on the faults is removed from this illustration because this steady motion is explicitly included in our deformation models as described in the previous section. The viscoelastic cycle model predicts relatively small vertical transient motions of 1 mm/yr or less in the region of interest for this study. We ignore this source of vertical motion for the remainder of this study.

Another source of vertical motion to consider is glacial isostatic adjustment (GIA). Figure 5c shows the predicted vertical motion in southern California from the Peltier (2004) radially-symmetric, viscoelastic, global model of surface uplift in response to

deglaciation. The model predicts broad tilting across southern California of order 0.5 mm/yr over several hundreds of kilometers. Other GIA models using different ice histories and/or Earth rheologies predict different rates of vertical deformation rate in southern California ranging from -1.8 to -0.2 mm/yr, with similarly low spatial gradients (Dalrymple et al., 2012).

Rapid basin subsidence due to sediment compaction in the Ventura and Los Angeles basins is also likely to be observed in the present-day deformation field. As discussed by Nicholson et al. (2007), sediment compaction can produce vertical and horizontal surface motions across basins that may look like deep fault slip or elastic strain accumulation. To account for this effect, we model sediment compaction assuming that the rate of present-day compaction can be derived from the compaction curve shown in Figure 6b, which is based on data in Nicholson et al. (2007) and McCulloh (1967). The compaction curve gives porosity as a function of depth, *p(z)*. We assume the basin is subsiding at a uniform rate with depth (but laterally variable), *dz/dt*. Then, by the chain rule, porosity reduction rate at a given depth is

$$\frac{dp(z)}{dt} = \frac{dp}{dz}\frac{dz}{dt}. \quad (3)$$

We obtain the gradient in porosity with depth, dp/dz, by differentiating the compaction curve (Figure 6b). The tectonic subsidence rate, dz/dt, is given by the depth to the 5 Ma surface in Figure 6a or the 1 Ma surface in Figure S4 divided by the age of the surface. We populate the volume of the sedimentary basin (Figure 6a) with a regular grid of centers of dilatation in an elastic halfspace (Mogi, 1958) and impose volumetric rate change using equation (3).

Figure 6c shows the computed surface displacement rate for this model using the 5 Ma surface. The model predicts surface subsidence rates of 2-3 mm/yr and horizontal contraction rates of up to about 2 mm/yr throughout the Ventura basin. About 1-2 mm/yr of surface subsidence and about 1 mm/yr of horizontal contraction is predicted in the Los Angeles basin. The 5 Ma surface probably exaggerates the spatial extent of the actively compacting sedimentary basins in this region. Figure S4 shows the predicted surface deformation for a model using the 1 Ma surface in the Ventura basin from Yeats (1981)

and Sorlien and Nicholson (2015). The rates of subsidence and contraction are similar in this model, but the deformation has a narrower spatial distribution with most of the contraction occurring offshore across the Ventura Basin.

Of the considered candidate deformation sources, in the following analyses we incorporate only those that are best resolved and have spatial patterns that correspond to the observed geodetic deformation rates of Figure 2b. The San Joaquin Valley load in Figure 4 is readily modeled, so we subtract that modeled deformation signal from the observed vertical signal and use this residual signal (Figure 4c) in all inversions in this paper. As stated previously, vertical velocities predicted by the viscoelastic cycle model (Figure 5) or relatively low (<1 mm/yr) and do not match the observed geodetic pattern (Figure 4c), thus we ignore transient viscoelastic mantle flow in this study. The predictions from the GIA models indicate modest (<0.5 m/yr) gradients in vertical rate over the hundreds of kilometers of our study area, so we ignore the contribution of GIA in the remainder of this study. However, modeled surface deformation due to basin compaction (Figure 6c) produces subsidence along the Santa Barbara coast and within the onshore Ventura Basin, similar to what is observed, suggesting compaction may contribute to the present-day vertical signal. We conduct inversions with and without this basin compaction effect in this study.

5. Results

We conducted three different inversions: (1) Straight fault geometry (Figure 1c) for the Ventura-Pitas Point fault without basin compaction, (2) Ramp-flat fault geometry for the Ventura-Pitas Point fault without basin compaction, and (3) Ramp-flat fault geometry for the Ventura-Pitas Point fault with basin compaction. Results presented in the following figures are for inversions (1) and (2). We briefly discuss inversion (3) after presentation of the other results.

The estimated mean and standard deviation of slip rate and locking depth are provided in the supplementary materials (Table S1) for all three inversions. The estimates of fault slip rates for inversions (1) and (2) are summarized in Figure 7 with the straight fault geometry inversion shown in parentheses when this rate is significantly different from the inversion using the ramp-flat fault geometry. The mean slip rates are similar for the two inversions except that the straight Ventura-Pitas Point fault inversion (1) places lower slip rates on the Ventura-Pitas Point fault and higher rates on the Red Mountain fault. The left-lateral slip rates are highest through the Ventura Basin. The strike-slip rate on the Ventura-Pitas Point system is at the upper end of the bounds at 2.9-3 mm/yr. The reported slip rate range is the 95% confidence interval. The summed left-lateral rate across the Santa Barbara Channel faults at longitude 119°30' is approximately 5 mm/yr. This is similar to the ~6 mm/yr rate across on the onshore Ventura Basin-bounding faults (Ventura and Oakridge Faults). The Ventura-Pitas Point fault system shows the highest dip-slip rate in the model with 4.4-5.2 mm/yr (2.8-3.6 mm/yr for the straight fault model) across the onshore portion and 1.9-2.7 mm/yr (0-3 mm/yr) offshore. The summed reverse-slip rates across several N-S profiles are shown in Figure 7b.

Figures 8-10 compare model predictions with data for the ramp-flat geometry inversion (inversion 2). The inversion inflates the formal uncertainties on all of the data sets; the data weights (σ in equation 1) are 3.6 for horizontal GPS data, 2.3 for the vertical geodetic data, and 3.5 for the geologic uplift data. The fit to the horizontal velocities are shown in Figure 8 and the residuals (observed minus model) are shown in Figure S2. To illustrate the amount of shortening across the region absorbed by reverse slip on faults, Figure 8b shows the modeled and observed horizontal velocity field after subtracting the modeled strike-slip contribution from all faults. Comparing Figure 8b with Figure 8a, it is clear that a large portion of the geodetic signal in this region is attributed to shortening across dipping faults. In fact, elastic strain due to coupling across the San Andreas and Garlock faults, which is included in the velocity field in Figure 8b, but not in Figure 8a, appears to mask some of the ~N-S shortening across the WTR. There is a slight systematic misfit across the Santa Barbara Channel indicating that the model underpredicts the shortening rate by 1-3 mm/yr.

A comparison between the observed and predicted vertical geodetic data is shown in Figure 9. The model does not capture all details of the observations, but most of the observed long-wavelength signal (50-100 km) is reproduced by the model. The model captures the 1-2 mm/yr of present-day subsidence along the Santa Barbara coastline and within the L.A. Basin as well as the general pattern of present-day interseismic uplift of the Santa Ynez Range and San Gabriel Mountains of 1-2 mm/yr. The general pattern of long-term predicted motion also matches the geologic vertical data fairly well (Figure 10). The model predicts 1-3 mm/yr of long-term subsidence in the off shore Ventura Basin, ~3 mm/yr of long-term subsidence in the onshore Ventura Basin and Santa Barbara Coast uplift of about 1 mm/yr, which are all in agreement with observations. The very high observed uplift rates (4-6 mm/yr) in the vicinity of the Ventura Avenue Anticline are not reproduced by the model (2-3 mm/yr).

It is not immediately obvious from examination of Figure 9 how the various faults contribute to the total vertical velocity field. To help make this clearer, we illustrate the contribution from only the Ventura-Pitas Point fault (ramp-flat geometry) in Figure 11. We see that this fault produces 1-2 mm/yr of long-term uplift north of the fault and 1-2 mm/yr of subsidence directly south of the fault (Figure 11b). Interseismic coupling on the fault (Figure 11c), modeled as backslip, produces mostly subsidence on the hanging wall side north of the fault trace. Adding together these two velocity fields, we see interseismic subsidence along the Santa Barbara coast (Figure 11d) and interseismic uplift north of the trace of the Mission Ridge/Arroyo Parida fault.

Many of the locking depths are not well resolved by the inversion. The upper and lower locking depths that are at best resolved are shown in Figure S3. The important result for this study is that the faults dipping underneath the Santa Barbara coastline including the Ventura-Pitas Point, Red Mountain, and North Channel West faults are locked to 10-20 km depth. The interseismic locking on these faults produces the observed interseismic subsidence along the Santa Barbara coast as illustrated for the Ventura-Pitas Point fault in Figure 11.

Figure 12 shows the fit to the data along profile A-A' (Figure 1a) for the straight fault model (1) and the ramp-flat model (2) without basin sediment compaction. Both models fit the geodetic data largely within uncertainties and most of the geologic, long-term data are fit within uncertainties (except near the Ventura Avenue Anticline). There is a tendency for the straight-fault model (green points in Figure 12) to under predict the uplift north (right) of the LMA, whereas the ramp-flat model (red points) matches the observed uplift well.

6. Discussion

The purpose of this study was to examine the present-day rates of deformation across the Western Transverse Ranges in the context of what is known about the geology of the active fold-thrust belt, including the geometry of known active faults, compaction of sediments in the very deep and rapidly subsiding Ventura basin, and Quaternary rates of uplift or exhumation across the region. One challenge in doing this is deciphering how much of the present-day vertical deformation recorded with geodetic data reflects recoverable, elastic deformation and how much reflects long-term, geologic vertical motions. This requires the development of a suitable deformation model that can account for the recoverable elastic deformation and longer-term, permanent motions. The kinematic model adopted for this study allows for long-term rigid and non-rigid motions of fault-bounded blocks of crust due to imposed long-term slip rates on faults. Long-term strain within the blocks of crust due to geometric complexities and flexure across dipping faults is approximated with deformation in an elastic plate over an inviscid substrate. We do not explicitly account for anelastic (plastic) yielding that would certainly be required in areas of high stress accumulation. While the lack of explicit treatment of anelasticity, other than sediment compaction in the basin, is a limitation of this study, it will likely not impact our primary conclusions regarding the relationships between known fault structures, interseismic strain and long term uplift.

Figure 12 places the geodetic data and results of the inversions within the context of the regional geologic cross section along the profile AA' in Figure 10 (previously shown in Figure 1c). Figure 12b-d compares the observed and predicted horizontal and vertical velocities along the profile for both versions of the Ventura fault geometry (green = straight fault, red = ramp-flat fault). We see that the ~19 mm/yr of relative horizontal motion is captured by the model (note that this is not all shortening, but includes lateral motion across the San Andreas Fault). Figure 12c shows that the general upward-arching pattern of interseismic vertical motion across the Santa Ynez Mountains is captured by both models, although the flat-ramp Ventura fault geometry (red dots) better captures the ~3 mm/yr over 30 km tilt observed from the coast (VAA) to the Santa Ynez Anticlinorium. This upward-arching vertical pattern is not seen in the observed and modeled long-term uplift pattern shown in Figure 12d. In the long-term we see ~2 mm/yr of uplift near the coast (higher across the VAA) that decreases to <1 mm/yr across the Santa Ynez Mountains to the north. The upward arching interseismic pattern in the model is a result of intersesimic locking along reverse faults near and south of the Santa Barbara coastline, and deep creep at depth on these faults, like illustrated in the idealized 2D fault models shown in Figure 3b. Thus, even though interseismic motion is now generally observed to be downward, our model predicts that coseismic thrusting on the Ventura-Pitas Point fault will raise the coastline, and cumulative earthquakes will continue to uplift the Santa Barbara coast over the long term.

Figure 13 summarizes the estimates of slip rates on major faults in the region and compares with assumed bounds and estimates from the forward mechanical models of Marshall et al. (2013) and Marshall et al. (2017) for three different fault geometries. The yellow bars in Figure 13 capture the entire range of estimates (at 95% confidence level) from the various inversions in this study. In most cases, the maximum model estimate is lower than the upper bound, suggesting the assumed upper bounds are not overly restrictive. The Northridge and Red Mountain faults are the only exceptions to this. The inversion results generally agree well with the Marshall et al. (2013; 2017) forward modeling results.

The Ventura-Pitas Point fault itself accounts for a large fraction of the potential moment release across the WTR. To show this, we compute posterior probability density functions of moment accumulation rate on faults for the ramp-flat inversion without basin compaction (inversion 2), as shown in Figure 14. Moment accumulation rate is computed from the posterior distributions of backslip rate and area of locking assuming an elastic shear modulus of 30 GPa. Here we show moment accumulation rates for all faults in the model and also separately for the Ventura-Pitas Point fault as well as geographic regions delineated in the inset in Figure 14a. The moment accumulation rate in the Santa Barbara channel region is similar to the on-shore moment accumulation rate in the LA Basin-San Fernando Valley. The total moment accumulation rate for all faults is about seven times higher and is dominated by moment accumulation rate on the San Andreas fault. We also convert moment accumulation rate to equivalent moment magnitude (M_w) per 100 and 1000 years in Figure 14. These results suggest there is enough moment accumulation to result in a M_w=7 earthquake on the Ventura-Pitas Point fault every 100 years and enough moment accumulation for about two M_w=7 events every 100 years in both the entire Santa Barbara Channel and the combined Los Angeles basin and San Fernando Valley regions. The estimated moment rate is broadly consistent with geologic estimates of past earthquakes on the Ventura fault system with magnitudes $M_w > 7.5$ occurring at intervals of ~1-4 ka (McAuliffe et al., 2015; Rockwell et al., 2016). Thus the Ventura-Pitas Point fault itself accounts for about half of the moment release in the greater Santa Barbara channel area, and about a quarter of that in the combined Santa Barbara Channel/LA Basin-San Fernando Valley areas shown in Figure 14.

The effect of modeled basin compaction on estimates of fault slip rates is modest (inversion 3). Slip rate estimates from this inversion are very similar to the ramp-flat geometry inversion without basin compaction (inversion 2). The main difference is that inversion (3) requires less coupling on the Ventura-Pitas Point Fault system and correspondingly lower moment accumulation rate by a factor of about two, as in Figure S5. The explanation for this is straightforward; model subsidence due to basin compaction along the Santa Barbara coastline (Figure 6c) accounts for about half of the observed present-day subsidence, requiring less subsidence due to interseismic strain

accumulation on the Ventura-Pitas Point Fault (Figure 11c and Figure S5c,d). However, we suspect that the basin compaction model adopted for this inversion constrained by the ~5 Ma SCEC basement model is likely an extreme end-member model as the modeled basin area is near the maximum allowable size approximating the actual basin.

Howell et al. (2016) constructed a vertical velocity field for southern California using continuous GPS data after filtering out short wavelength signals they attributed to non-tectonic sources. Their filtered velocity field shows several mm/yr of roughtly N-S tilt across the Western Transverse Ranges, similar to, but not exactly as seen in the data adopted for this study (Hammond et al., 2018). Howell et al. (2016) attribute this and other signals across southern California to interseismic coupling and deep creep associated with the earthquake cycle on the San Andreas fault. While their model does indeed capture some first order features of the vertical velocity field across southern California, it does not reproduce the N-S tilt across the Western Transverse Ranges. Howell et al. (2016) did not include vertical motions due to dip-slip faulting in this region, and this is likely the reason for the misfit.

As noted in the discussion of fit to long-term data in Figure 12d, our model does not capture the highly localized uplift across the Ventura Avenue Anticline captured in the Niemi et al. (2008) data set. Similarly high localized uplift rates of 6-7 mm/yr have also been recorded across the anticline by Rockwell et al. (2016) from folded Holocene marine terraces. These high uplift rates presumably reflect highly localized deformation associated with anelastic folding processes that are not accounted for in our simplified elastic models. Furthermore, for simplicity we have not allowed for large slip rate gradients along fault segments that would likely be required to produce such high slip rates. Marshall et al. (2017) showed that boundary element models are capable of producing locally high slip rates approaching 7 mm/yr in the vicinity of the Ventura Avenue Anticline.

7. Conclusions

In this paper, we combined geologic measurements of uplift rate with geodetic measurements of present-day vertical and horizontal motions into a single model for recent deformation across the Western Transverse Range fold-thrust belt. The kinematic model consists of faults embedded in an elastic layer (crust) subjected to gravitational restoring forces overlying an inviscid substrate (mantle). We inverted for slip rate on faults and interseismic locking area. The model captures the first-order features of the long-term geologic vertical motions and geodetic data.

We show that a large component of the vertical geodetically-derived velocity field is tectonic in nature. We attribute most of the uplift signal to interseismic strain accumulation from dip-slip motion on faults. The summed reverse slip rates on faults across the Western Transverse Ranges range from 11-15 mm/yr in the eastern Santa Barbara Channel and onshore Ventura regions to 5-6 mm/yr in the western Santa Barbara Channel region. These faults simultaneously and cumulatively accommodate 5 mm/yr of left-lateral motion inclusive of, and north of, the Channel Islands.

We resolve a key puzzle in vertical motions on the Santa Barbara coast, where long-term uplift is observed, but geodetically measured motions are downward. We find that the observed 3-4 mm/yr tilt from the Santa Barbara coastline to the Santa Ynez mountains is attributable to recoverable elastic deformation (not permanent) on north dipping thrusts. The model predicts interseismic subsidence along the Santa Barbara coastline and ~2 mm/yr long-term uplift in the Santa Ynez Range, and coseismic uplift of the Santa Barbara coastline in future large slip events.

The slip rates we infer are consistent with relatively high moment accumulation rates on faults in the WTR. The moment accumulation rate on the Ventura-Pitas Point fault system is equivalent to a M_w=7 earthquake every 100 years. The total moment accumulation rate in both the Santa Barbara Channel and the combined San Fernando Valley-LA Basin region is equivalent to about two M_w=7 earthquakes every 100 years.

8. Acknowledgements

The geodetic data used in this study were published in Hammond et al. (2018). All of the geodetic data, the geologic vertical rates from Niemi et al. (2008), and the ~1Ma horizon from Sorlien and Nicholson (2015) can be download form IUScholarWorks, Indiana University's open access repository at the following link: http://hdl.handle.net/2022/25234. This work was supported by the Southern California Earthquake Center (SCEC, #14055). This is SCEC contribution number 8165.

9. References

Amos, C. B., Audet, P., Hammond, W. C., Bürgmann, R., Johanson, I. A., and Blewitt, G., 2014, Uplift and seismicity driven by groundwater depletion in central California: Nature, v. 509, no. 7501, p. 483-486.

Argus, D. F., Landerer, F. W., Wiese, D. N., Martens, H. R., Fu, Y., Famiglietti, J. S., Watkins, M. M., 2017, Sustained water loss in California's mountain ranges during severe drought from 2012 to 2015 inferred from GPS. Journal of Geophysical Research: Solid Earth, 122, 10,559–10,585. https://doi.org/10.1002/ 2017JB014424.

Beavan, J., Denys, P., Denham, M., Hager, B., Herring, T., and Molnar, P., 2010, Distribution of present‐day vertical deformation across the Southern Alps, New Zealand, from 10 years of GPS data: Geophysical Research Letters, v. 37, no. 16.

Borsa, A. A., Agnew, D. C., and Cayan, D. R., 2014, Ongoing drought-induced uplift in the western United States: Science, v. 345, no. 6204, p. 1587-1590.

Ching, K. E., Hsieh, M. L., Johnson, K. M., Chen, K. H., Rau, R. J., and Yang, M., 2011, Modern vertical deformation rates and mountain building in Taiwan from precise leveling and continuous GPS observations, 2000–2008: Journal of Geophysical Research: Solid Earth, v. 116, no. B8.

Clark, D., Hall, N., Hamilton, D., and Heck, R., 1991, Structural analysis of late Neogene deformation in the central offshore Santa Maria Basin, California: Journal of Geophysical Research: Solid Earth, v. 96, no. B4, p. 6435-6457.

Dalrymple, R. A., Breaker, L., Brooks, B., Cayan, D., Griggs, G., Han, W., Horton, B., Hulbe, C., McWilliams, J., and Mote, P., 2012, Sea-Level Rise for the Coasts of California, Oregon, and Washington: Past, Present, and Future: National Research, Council The National Academies Press, Washington DC.

Dawson, T. E., and Weldon, R. J., 2013, Appendix B: Geologic slip-rate data and geologic deformation model: US Geol. Surv. Open‐File Rept.

DeVries, P. M., Krastev, P. G., and Meade, B. J., 2016, Geodetically constrained models of viscoelastic stress transfer and earthquake triggering along the North

631 Anatolian fault: Geochemistry, Geophysics, Geosystems, v. 17, no. 7, p. 2700-
632 2716.
633 Donnellan, A., Hager, B. H., King, R. W., and Herring, T. A., 1993, Geodetic
634 measurement of deformation in the Ventura Basin region, southern
635 California: Journal of Geophysical Research: Solid Earth, v. 98, no. B12, p.
636 21727-21739.
637 Field, E. H., Arrowsmith, R. J., Biasi, G. P., Bird, P., Dawson, T. E., Felzer, K. R., Jackson,
638 D. D., Johnson, K. M., Jordan, T. H., and Madden, C., 2014, Uniform California
639 Earthquake Rupture Forecast, Version 3 (UCERF3)–The Time‐Independent
640 Model: Bulletin of the Seismological Society of America, v. 104, no. 3, p. 1122-
641 1180.
642 Fu, Y., Argus, D. F., and Landerer, F. W., 2015, GPS as an independent measurement
643 to estimate terrestrial water storage variations in Washington and Oregon:
644 Journal of Geophysical Research: Solid Earth, v. 120, no. 1, p. 552-566.
645 Fukuda, J. i., and Johnson, K. M., 2010, Mixed linear—non-linear inversion of crustal
646 deformation data: Bayesian inference of model, weighting and regularization
647 parameters: Geophysical Journal International, v. 181, no. 3, p. 1441-1458.
648 Gratier, J., Hopps, T., Sorlien, C., and Wright, T., 1999, Recent crustal deformation in
649 southern California deduced from the restoration of folded and faulted
650 strata: Journal of Geophysical Research: Solid Earth, v. 104, no. B3, p. 4887-
651 4899.
652 Hager, B. H., Lyzenga, G. A., Donnellan, A., and Dong, D., 1999, Reconciling rapid
653 strain accumulation with deep seismogenic fault planes in the Ventura basin,
654 California: Journal of Geophysical Research: Solid Earth, v. 104, no. B11, p.
655 25207-25219.
656 Hammond, W. C., Blewitt, G., and Kreemer, C., 2011, Block modeling of crustal
657 deformation of the northern Walker Lane and Basin and Range from GPS
658 velocities: Journal of Geophysical Research: Solid Earth, v. 116, no. B4.
659 Hammond, W. C., Blewitt, G., & Kreemer, C. , 2016, GPS Imaging of vertical land
660 motion in California and Nevada: Implications for Sierra Nevada uplift:
661 Journal of Geophysical Research: Solid Earth, v. 121, no. 10, p. 7681-7703.
662 Hammond, W. C., Burgette, R. J., Johnson, K. M., and Blewitt, G., 2018, Uplift of the
663 Western Transverse Ranges and Ventura Area of Southern California: A
664 Four‐Technique Geodetic Study Combining GPS, InSAR, Leveling, and Tide
665 Gauges: Journal of Geophysical Research: Solid Earth, v. 123, no. 1, p. 836-
666 858.
667 Hornafius, J. S., Luyendyk, B. P., Terres, R., and Kamerling, M., 1986, Timing and
668 extent of Neogene tectonic rotation in the western Transverse Ranges,
669 California: Geological Society of America Bulletin, v. 97, no. 12, p. 1476-1487.
670 Howell, S., Smith-Konter, B., Frazer, N., Tong, X., and Sandwell, D., 2016, The vertical
671 fingerprint of earthquake cycle loading in southern California: Nature
672 Geoscience, v. 9, no. 8, p. 611-614.
673 Huang, W. J., Johnson, K. M., Fukuda, J. i., and Yu, S. B., 2010, Insights into active
674 tectonics of eastern Taiwan from analyses of geodetic and geologic data:
675 Journal of Geophysical Research: Solid Earth, v. 115, no. B3.

676 Hubbard, J., Shaw, J. H., Dolan, J., Pratt, T. L., McAuliffe, L., and Rockwell, T. K., 2014,
677 Structure and seismic hazard of the Ventura Avenue anticline and Ventura
678 fault, California: Prospect for large, multisegment ruptures in the western
679 Transverse Ranges: Bulletin of the Seismological Society of America.
680 Huftile, G. J., and Yeats, R. S., 1995, Convergence rates across a displacement transfer
681 zone in the western Transverse Ranges, Ventura basin, California: Journal of
682 Geophysical Research: Solid Earth, v. 100, no. B2, p. 2043-2067.
683 Jackson, J., and Molnar, P., 1990, Active faulting and block rotations in the western
684 Transverse Ranges, California: Journal of Geophysical Research: Solid Earth,
685 v. 95, no. B13, p. 22073-22087.
686 Johnson, K., Segall, P., and Yu, S., 2005, A viscoelastic earthquake cycle model for
687 Taiwan: Journal of Geophysical Research: Solid Earth, v. 110, no. B10.
688 Johnson, K. M., 2013, Slip rates and off‐fault deformation in Southern California
689 inferred from GPS data and models: Journal of Geophysical Research: Solid
690 Earth, v. 118, no. 10, p. 5643-5664.
691 Johnson, K. M., and Fukuda, J. i., 2010, New methods for estimating the spatial
692 distribution of locked asperities and stress‐driven interseismic creep on
693 faults with application to the San Francisco Bay Area, California: Journal of
694 Geophysical Research: Solid Earth, v. 115, no. B12.
695 Kamerling, M. J., and Luyendyk, B. P., 1985, Paleomagnetism and Neogene tectonics
696 of the northern Channel Islands, California: Journal of Geophysical Research:
697 Solid Earth, v. 90, no. B14, p. 12485-12502.
698 Luyendyk, B. P., and Hornafius, J. S., 1987, Neogene crustal rotations, fault slip, and
699 basin development in southern California, Prentice Hall, New York.
700 Marshall, S. T., Funning, G. J., Krueger, H. E., Owen, S. E., and Loveless, J. P., 2017,
701 Mechanical models favor a ramp geometry for the Ventura‐pitas point fault,
702 California: Geophysical Research Letters, v. 44, no. 3, p. 1311-1319.
703 Marshall, S. T., Funning, G. J., and Owen, S. E., 2013, Fault slip rates and interseismic
704 deformation in the western Transverse Ranges, California: Journal of
705 Geophysical Research: Solid Earth, v. 118, no. 8, p. 4511-4534.
706 McAuliffe, L. J., Dolan, J. F., Rhodes, E. J., Hubbard, J., Shaw, J. H., and Pratt, T. L., 2015,
707 Paleoseismologic evidence for large-magnitude (Mw 7.5–8.0) earthquakes on
708 the Ventura blind thrust fault: Implications for multifault ruptures in the
709 Transverse Ranges of southern California: Geosphere, v. 11, no. 5, p. 1629-
710 1650.
711 McCaffrey, R., 2005, Block kinematics of the Pacific–North America plate boundary
712 in the southwestern United States from inversion of GPS, seismological, and
713 geologic data: Journal of Geophysical Research: Solid Earth, v. 110, no. B7.
714 McCulloh, T. H., 1967, Mass properties of sedimentary rocks and gravimetric effects
715 of petroleum and natural-gas reservoirs: U.S. Geological Survey Professional
716 Paper, v. 528-A, p. 50.
717 Meade, B. J., and Hager, B. H., 2005a, Block models of crustal motion in southern
718 California constrained by GPS measurements: Journal of Geophysical
719 Research: Solid Earth, v. 110, no. B3.

720 Meade, B. J., & Hager, B. H. , 2005b, Spatial localization of moment deficits in
721 southern California: Journal of Geophysical Research: Solid Earth, v. 110, no.
722 B4.
723 Mogi, K., 1958, Relations between the eruptions of various volcanoes and the
724 deformations of the ground surfaces around them: Bulletin of the Earthquake
725 Research Institute of the University of Tokyo, v. 36, p. 99-134.
726 Namson, J., and Davis, T., 1988, Structural transect of the western Transverse
727 Ranges, California: Implications for lithospheric kinematics and seismic risk
728 evaluation: Geology, v. 16, no. 8, p. 675-679.
729 Nicholson, C., Kamerling, M. J., Sorlien, C. C., Hopps, T. E., and Gratier, J.-P., 2007,
730 Subsidence, compaction, and gravity sliding: implications for 3D geometry,
731 dynamic rupture, and seismic hazard of active basin-bounding faults in
732 Southern California: Bulletin of the Seismological Society of America, v. 97,
733 no. 5, p. 1607-1620.
734 Nicholson, C., Sorlien, C. C., Atwater, T., Crowell, J. C., and Luyendyk, B. P., 1994,
735 Microplate capture, rotation of the western Transverse Ranges, and initiation
736 of the San Andreas transform as a low-angle fault system: Geology, v. 22, no.
737 6, p. 491-495.
738 Niemi, N. A., Oskin, M., and Rockwell, T. K., 2008, Southern California earthquake
739 center geologic vertical motion database: Geochemistry, Geophysics,
740 Geosystems, v. 9, no. 7.
741 Peltier, W., 2004, Global glacial isostasy and the surface of the ice-age Earth: the ICE-
742 5G (VM2) model and GRACE: Annu. Rev. Earth Planet. Sci., v. 32, p. 111-149.
743 Plesch, A., Shaw, J. H., Benson, C., Bryant, W. A., Carena, S., Cooke, M., Dolan, J., Fuis,
744 G., Gath, E., and Grant, L., 2007, Community fault model (CFM) for southern
745 California: Bulletin of the Seismological Society of America, v. 97, no. 6, p.
746 1793-1802.
747 Pollitz, F. F., Wicks, C., and Thatcher, W., 2001, Mantle flow beneath a continental
748 strike-slip fault: Postseismic deformation after the 1999 Hector Mine
749 earthquake: Science, v. 293, no. 5536, p. 1814-1818.
750 Rockwell, T. K., Clark, K., Gamble, L., Oskin, M. E., Haaker, E. C., and Kennedy, G. L.,
751 2016, Large Transverse Range Earthquakes Cause Coastal Upheaval near
752 Ventura, Southern California: Bulletin of the Seismological Society of
753 America, v. 106, no. 6, p. 2706-2720.
754 Savage, J., and Prescott, W., 1978, Asthenosphere readjustment and the earthquake
755 cycle: Journal of Geophysical Research: Solid Earth, v. 83, no. B7, p. 3369-
756 3376.
757 Schneider, C. L., Hummon, C., Yeats, R. S., and Huftile, G. L., 1996, Structural evolution
758 of the northern Los Angeles basin, California, based on growth strata:
759 Tectonics, v. 15, no. 2, p. 341-355.
760 Shen, Z. K., King, R., Agnew, D., Wang, M., Herring, T., Dong, D., and Fang, P., 2011, A
761 unified analysis of crustal motion in Southern California, 1970–2004: The
762 SCEC crustal motion map: Journal of Geophysical Research: Solid Earth, v.
763 116, no. B11.

764 Smith, B. R., and Sandwell, D. T., 2006, A model of the earthquake cycle along the San
765 Andreas Fault System for the past 1000 years: Journal of Geophysical
766 Research: Solid Earth, v. 111, no. B1.
767 Smith‐Konter, B. R., Thornton, G. M., and Sandwell, D. T., 2014, Vertical crustal
768 displacement due to interseismic deformation along the San Andreas fault:
769 Constraints from tide gauges: Geophysical Research Letters, v. 41, no. 11, p.
770 3793-3801.
771 Sorlien, C. C., Gratier, J.-P., Luyendyk, B. P., Hornafius, J. S., and Hopps, T. E., 2000,
772 Map restoration of folded and faulted late Cenozoic strata across the Oak
773 Ridge fault, onshore and offshore Ventura basin, California: Geological
774 Society of America Bulletin, v. 112, no. 7, p. 1080-1090.
775 Sorlien, C. C., and Nicholson, C., 2015, Post-1 Ma deformation history of the Pitas
776 Point-North Channel-Red Mountain fault system and associated folds in the
777 Santa Barbara Channel: Final Report to U.S. Geological Survey NEHRP, no.
778 contract USDI/USGS G14AP00012, p. 24.
779 Sorlien, C. C., Nicholson, C., Behl, R. J., and Kamerling, M. J., 2016. Displacement
780 direction and 3D geometry for the south-directed North Channel – Pitas Point
781 fault system and north-directed ramps, decollements, and other faults
782 beneath Santa Barbara Channel, *in* Proceedings Southern California
783 Earthquake Center Annual Meeting, Palm Springs, CA, 2016, Volume XXVI.
784 Tape, C., Plesch, A., Shaw, J. H., and Gilbert, H., 2012, Estimating a continuous Moho
785 surface for the California unified velocity model: Seismological Research
786 Letters, v. 83, no. 4, p. 728-735.
787 Timoshenko, S., Timoshenko, S., and Goodier, J., 1951, Theory of Elasticity, by S.
788 Timoshenko and JN Goodier, McGraw-Hill book Company.
789 Yeats, R. S., 1981, Deformation of a 1 Ma Datum, Ventura Basin, California: U. S.
790 Geological Survey, Technical Report, v. Contract No. 14-08-0001-18283.
791 Yeats, R. S., 1983, Large‐scale Quaternary detachments in Ventura basin, southern
792 California: Journal of Geophysical Research: Solid Earth, v. 88, no. B1, p. 569-
793 583.
794 Zeng, Y., and Shen, Z.-K., 2014, Fault network modeling of crustal deformation in
795 California constrained using GPS and geologic observations: Tectonophysics,
796 v. 612, p. 1-17.
797
798

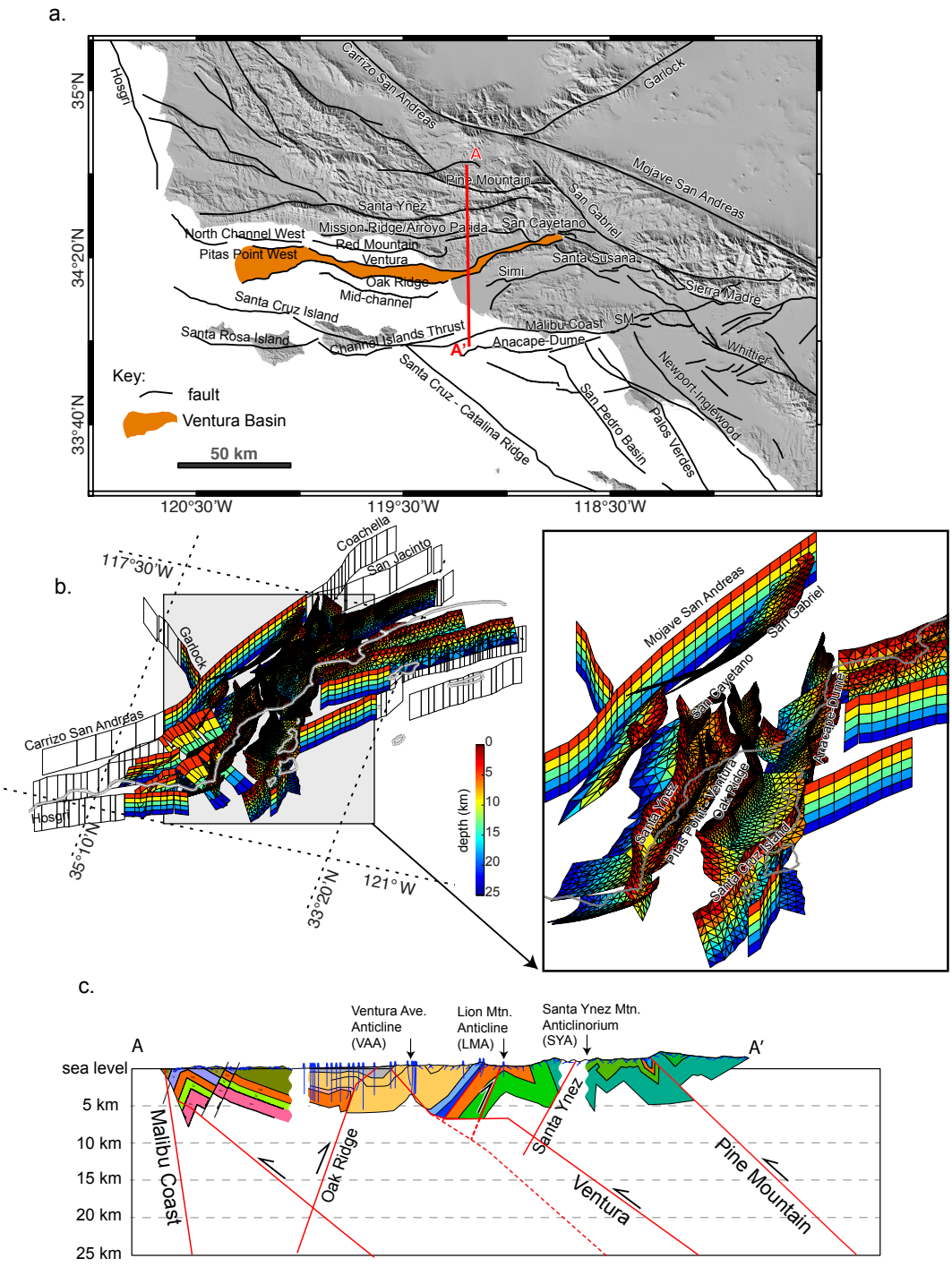

Figure 1. Fault geometry in Western Transverse Ranges, southern California. Geometry is a compilation from SCEC Community Fault Model (Plesch et al., 2007), UCERF3 fault model (Field et al., 2014), and Sorlien et al. (2016). (a) Map view of fault traces. (b) 3D perspective view of model faults and enlargement of Santa Barbara Channel region faults. Slip rates are estimated on colored fault surfaces and imposed on white faults. (c) Profile AA'. Shallow geology is from Namson and Davis (1988). Red lines show intersection of model faults with cross section. Dashed red line is alternative straight fault geometry for the Ventura Fault.

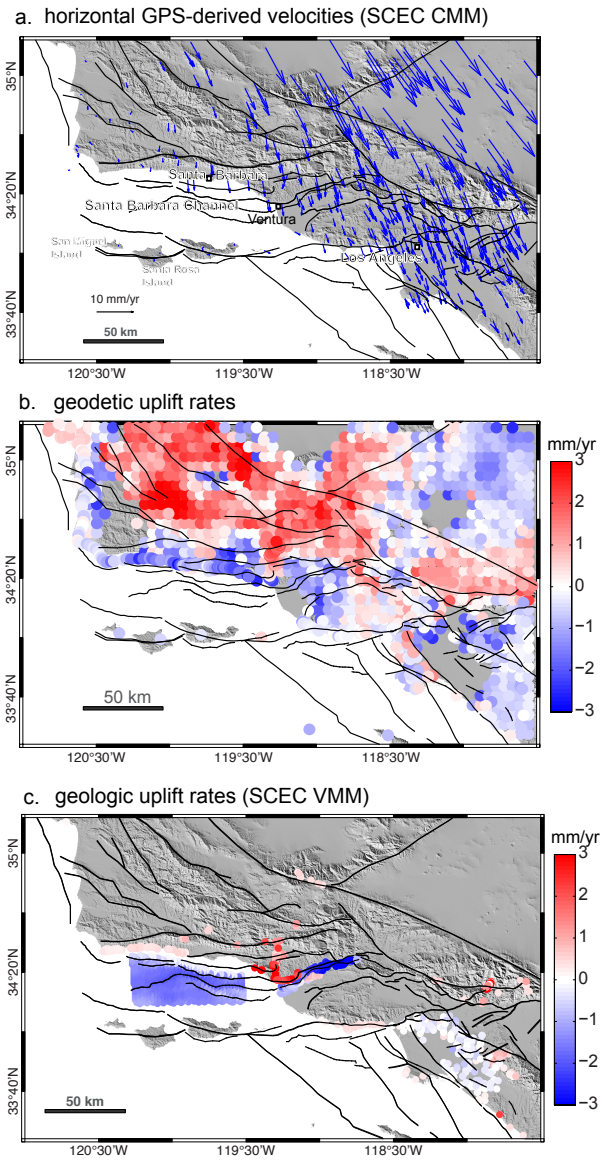

Figure 2. Geodetic and geologic data used to constrain inversions for fault slip rates and locking. (a) SCEC CMM4 velocity field relative to San Miguel/Santa Rosa Islands. (b) Present-day vertical motion map from a combination of InSAR, GPS, and leveling data (Hammond et al, 2018). (c) Geologic vertical motions from Niemi et al. (2008) and Sorlien and Nicholson (2015).

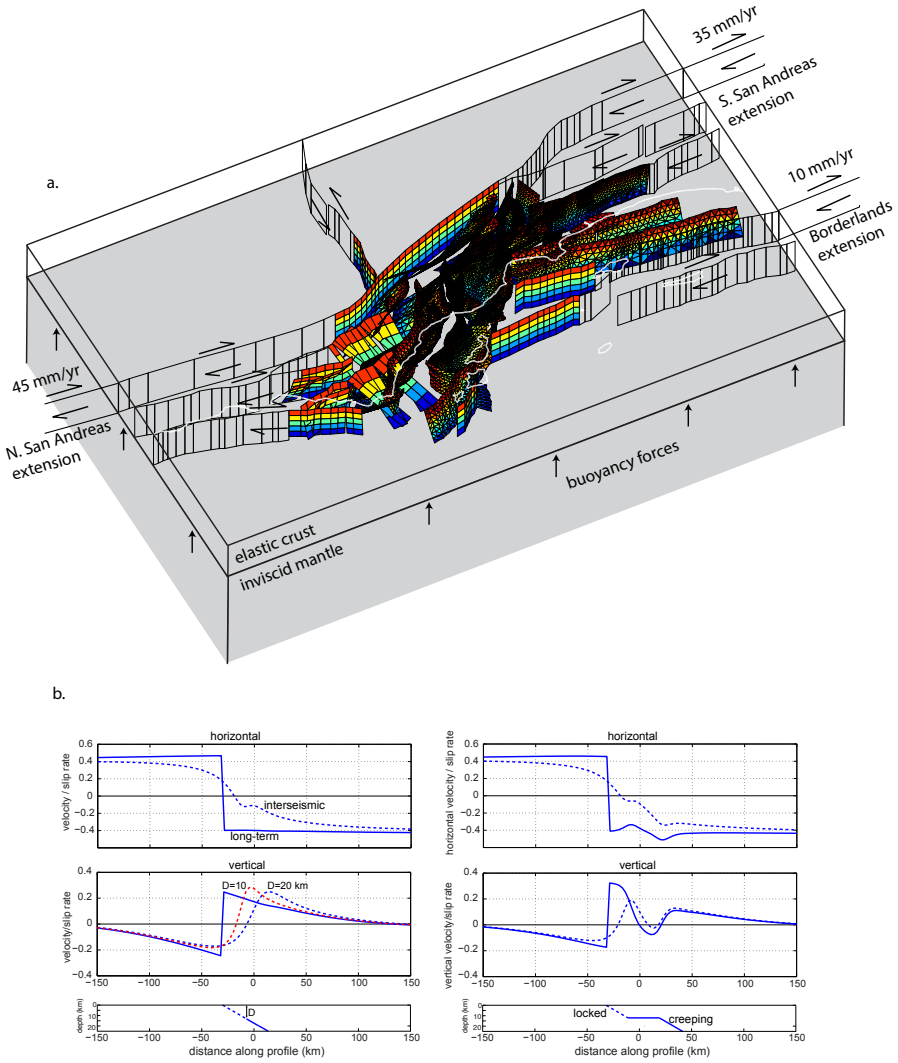

Figure 3. Illustration of elastic plate flexure model. (a) Faults are embedded in a 25-km-thick elastic crustal plate overlying an inviscid mantle. Elastic plate flexes under gravitational restoring forces (buoyancy forces) due to slip on faults. Slip is imposed on clear vertical fault panes (these faults extend to great distance outside of the shown model region to generate appropriate far-field horizontal plate motions). Slip rate on colored faults is solved for in the inversion. Uniform long-term slip rate is assumed over entire fault sections. In steady state deformation, over millennial time scales, faults creep at a constant rate and induce steady deformation. During the interseismic period, faults are assumed to be locked above some locking depth that is solved for in the inversion. Interseismic locking is modeled with backslip in an elastic halfspace. (b) Illustration of the analogous elastic plate flexure model in 2D, plane-strain case (infinitely long faults). Geometry of fault and plate is shown in lower panel with locked section of fault indicated with dashed line and interseismic creeping fault indicated with solid lines. Upper panels show predicted long-term (solid lines) and intersesimic (dashed) horizontal and vertical velocities normalized by slip rate on the fault. Locking depth is indicated by variable D.

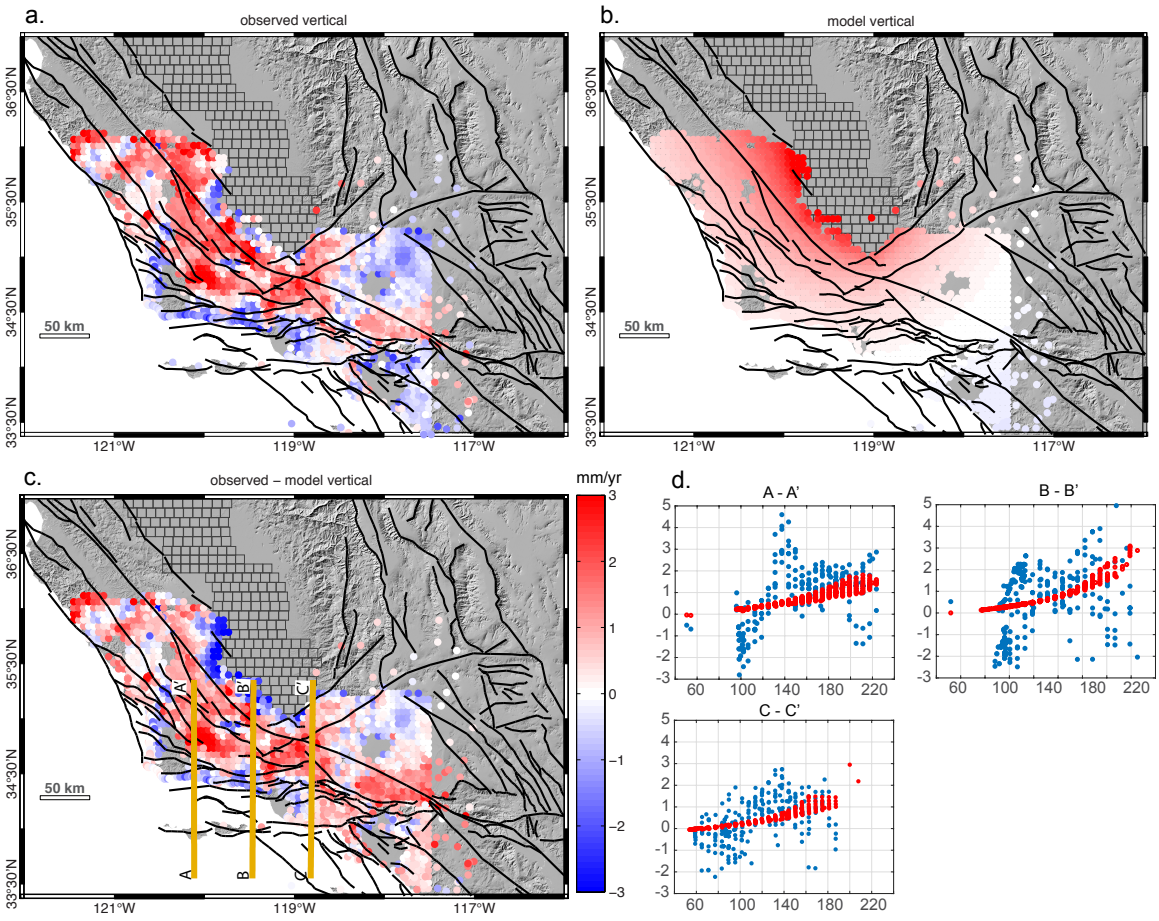

Figure 4. Estimate of vertical motions from withdrawal of water from San Joaquin Valley aquifers. (a) Observed vertical motions (same as Figure 1B). (b) Predicted vertical motions on top of elastic halfspace due to removal of water in San Joaquin Valley following approach of Amos et al. (2014). "Carrizo SAF" is Carrizo section of San Andreas Fault referred to in main text. (c) Vertical velocity field with contribution from water withdrawal (b) removed. (d) Profiles of observed (blue dots) and predicted (red dots) vertical velocities due to removal of water within 25 km of profile lines shown in (c). Predicted vertical velocities do not match the pattern of observed uplift/subsidence, indicating another source of vertical motion is involved in addition to the water unloading.

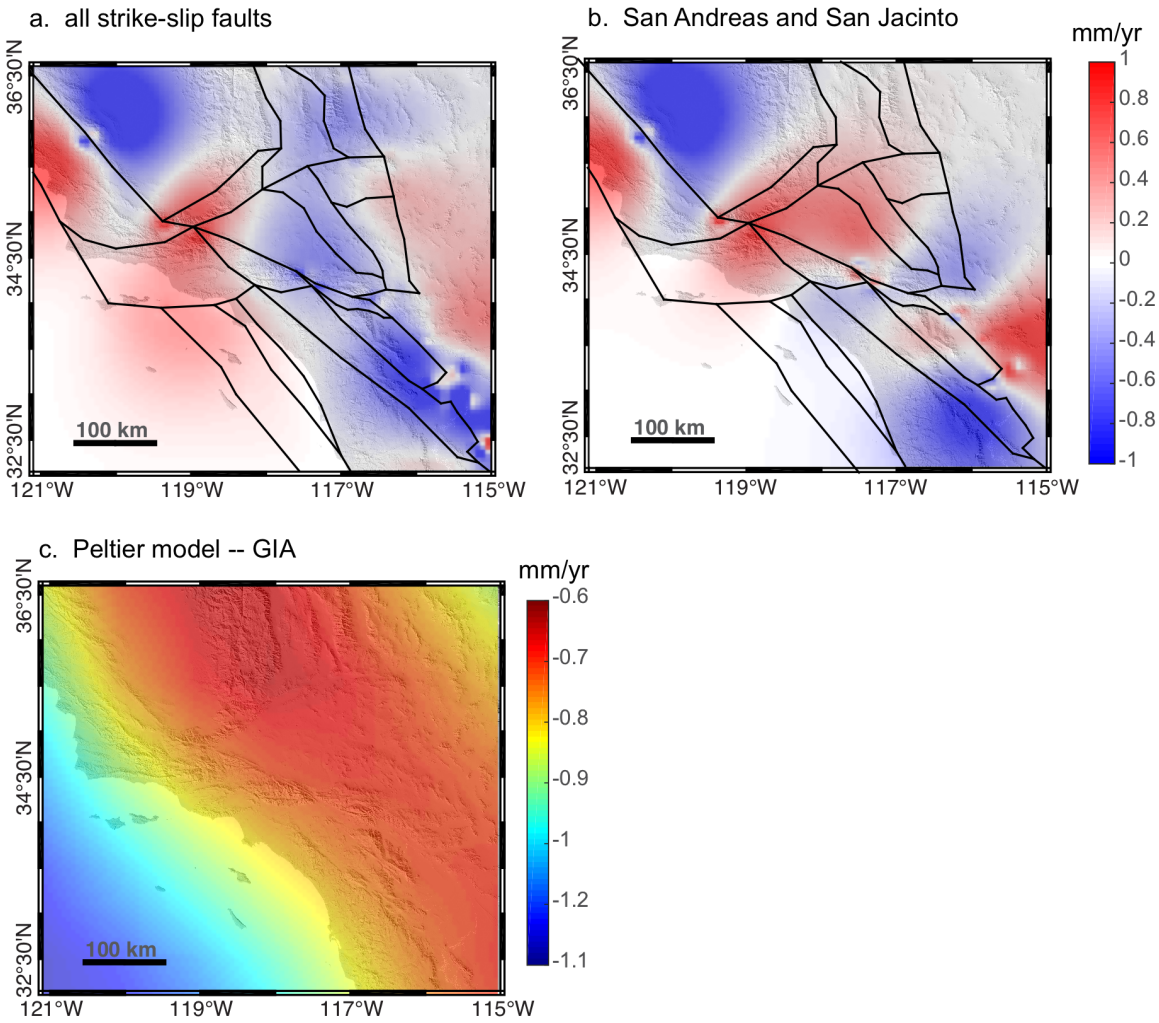

Figure 5. Viscoelastic models of vertical motion. a. Earthquake cycle model of Johnson (2013) showing transient contribution from earthquake cycle on strike-slip faults. b. Earthquake cycle model of Johnson (2013) showing transient contribution from earthquake cycle on San Andreas and San Jacinto Faults. c. Global post-glacial rebound (Glacial Isostatic Adjustment – GIA) model of solid earth vertical motions from Peltier (2004).

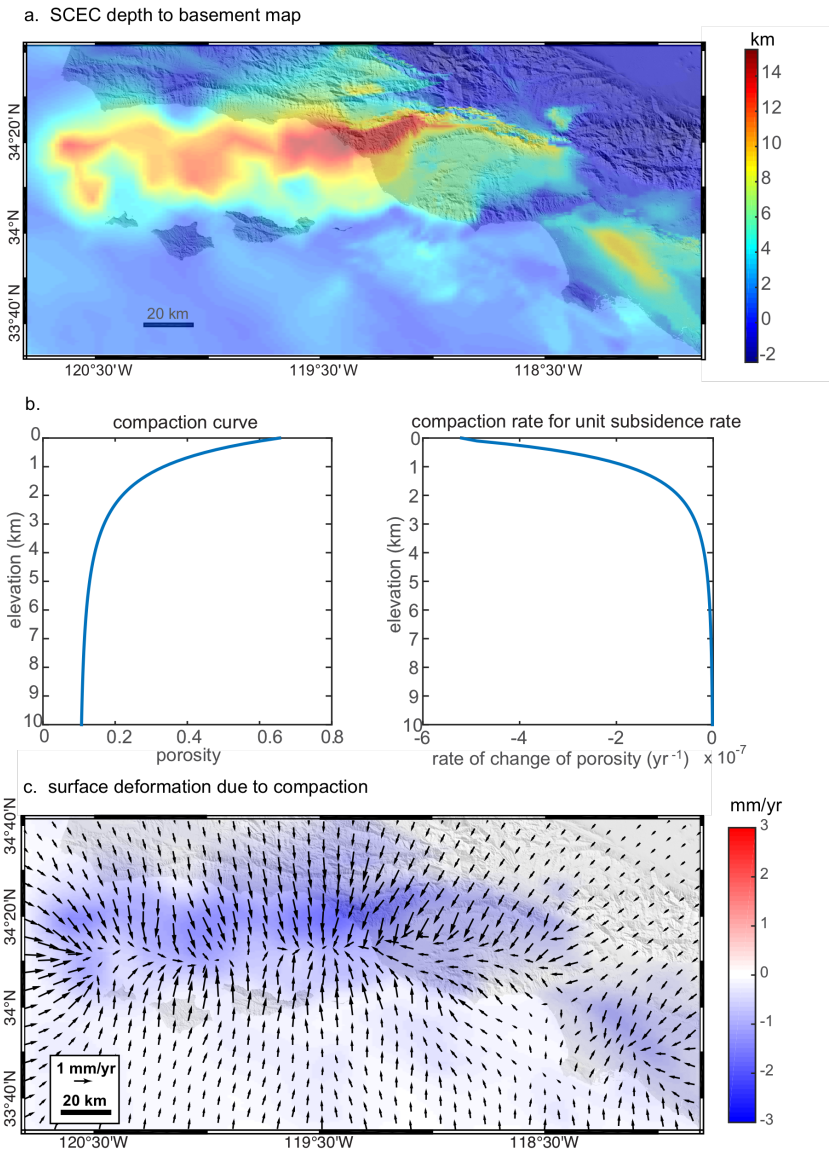

Figure 6. Calculated deformation due to sediment compaction. (a) SCEC basement depth map (5 Ma surface) . (b) Assumed compaction curve following McCulloh (1967) and Nicholson et al. (2007). Compaction rate as a function of depth assuming constant subsidence rate. (c) Predicted subsidence and horizontal velocities assuming compaction in an elastic half space.

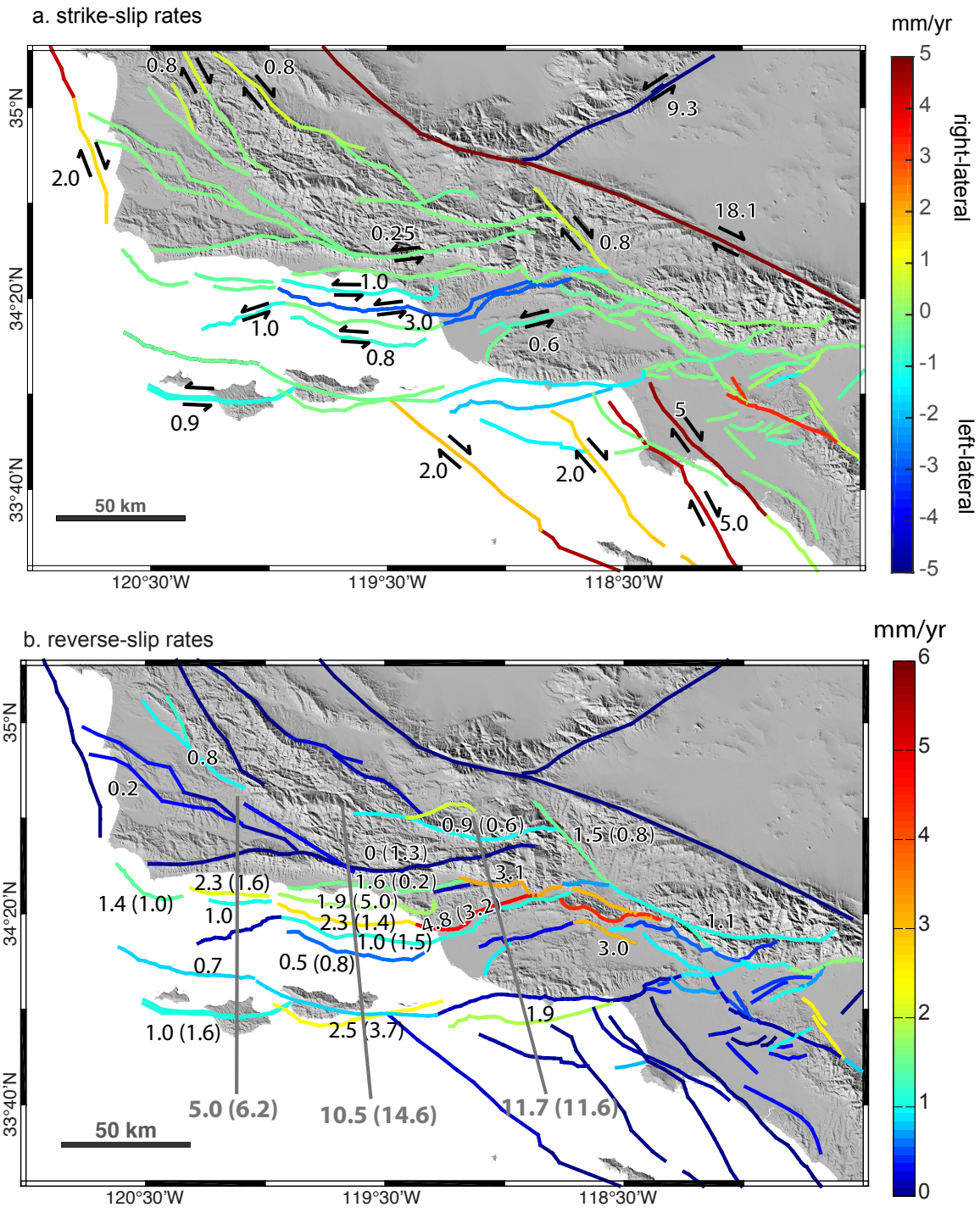

Figure 7. Estimated slip rates shown on surface fault traces. (a) Strike-slip component of slip rate. Positive is right-lateral and negative is left-lateral. (b) Dip-slip rate component. Numbers in parentheses are for the straight Ventura-Pitas Point model inversion and other numbers are for the ramp-flat geometry. All faults constrained to reverse sense of slip. Dip-slip rate is summed along faults crossing the three profile lines.

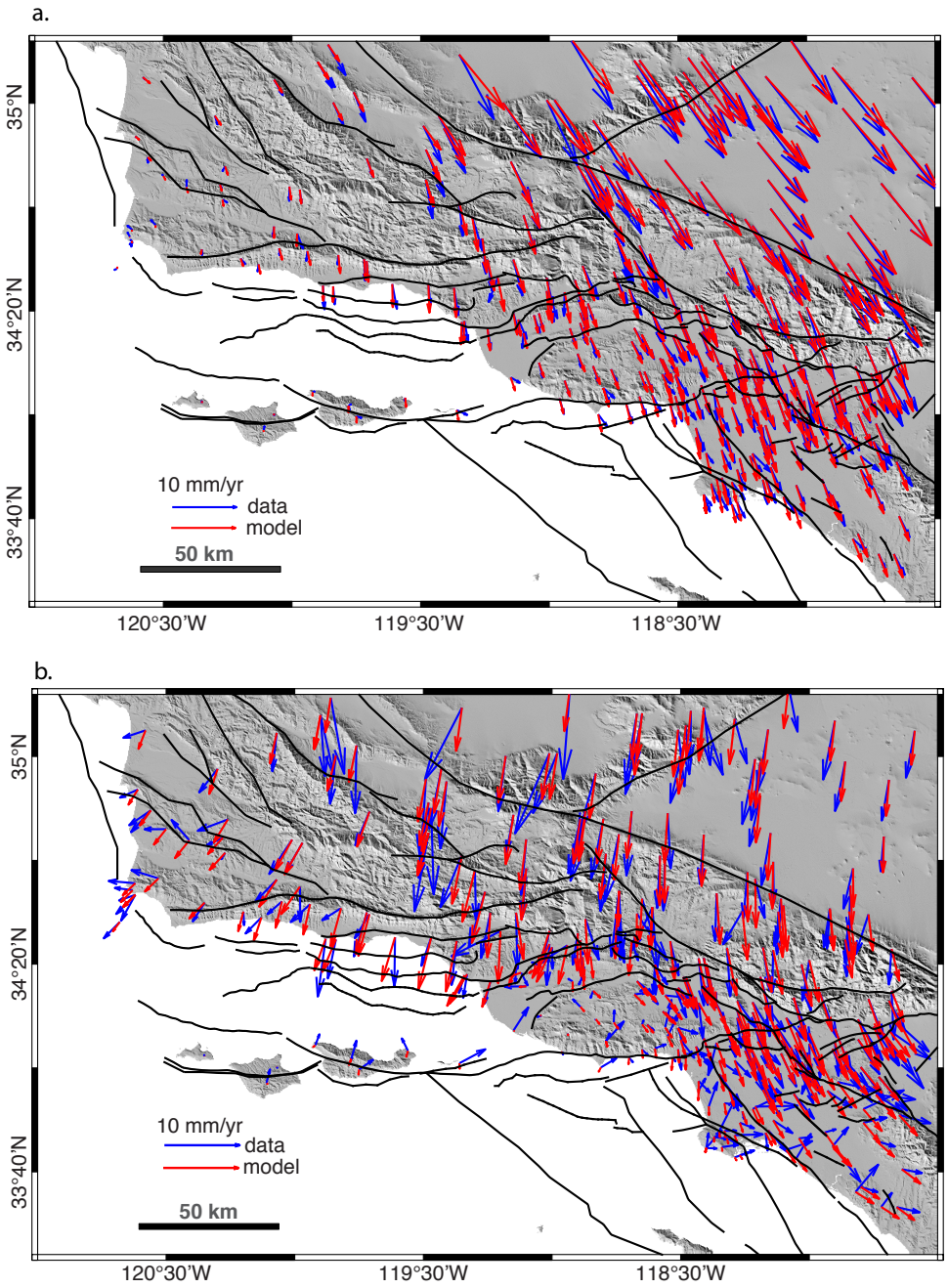

Figure 8. Observed and predicted horizontal velocities. (a) Total velocity field relative to San Miguel/Santa Rosa Islands. (b) Velocity field after removal of strike-slip contribution from all faults. This velocity field isolates the contribution to contraction due to slip on reverse faults.

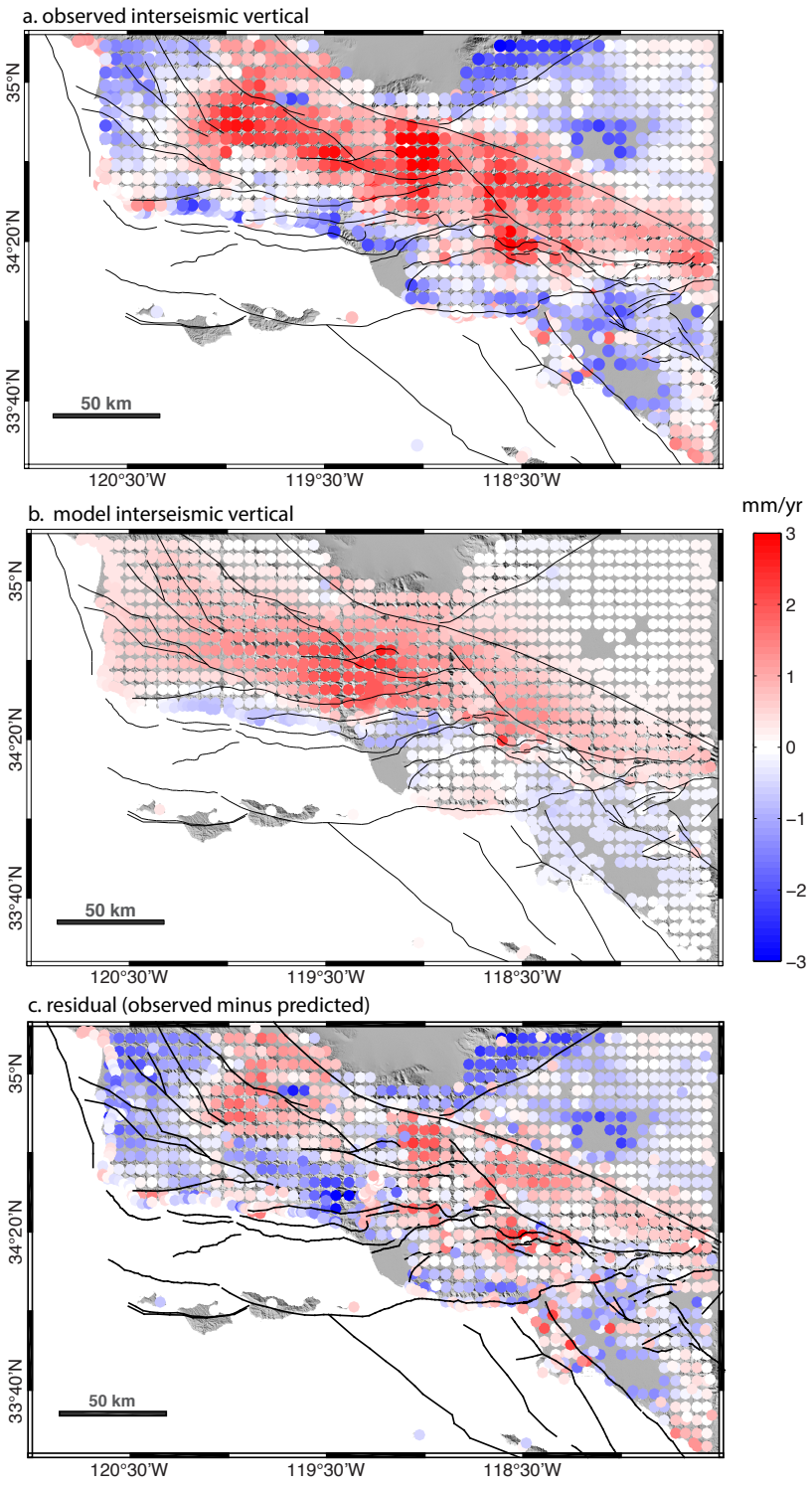

862
863 *Figure 9. Observed (a), predicted (b), and residual (c) interseismic vertical velocities.*

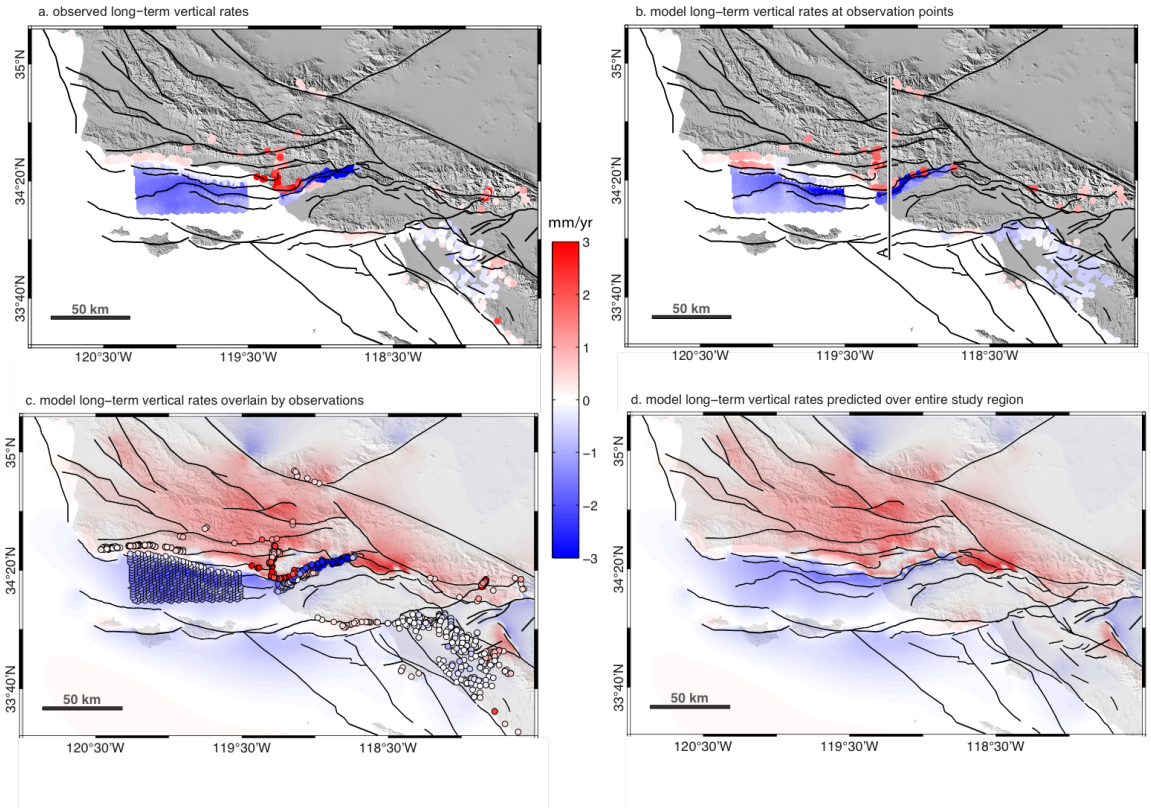

Figure 10. Comparison of observed and modeled long-term vertical. (a) observed, (b) model at observation points, (c) model long-term vertical rates over entire region compared with observations, and (d) model long-term vertical rates over entire region.

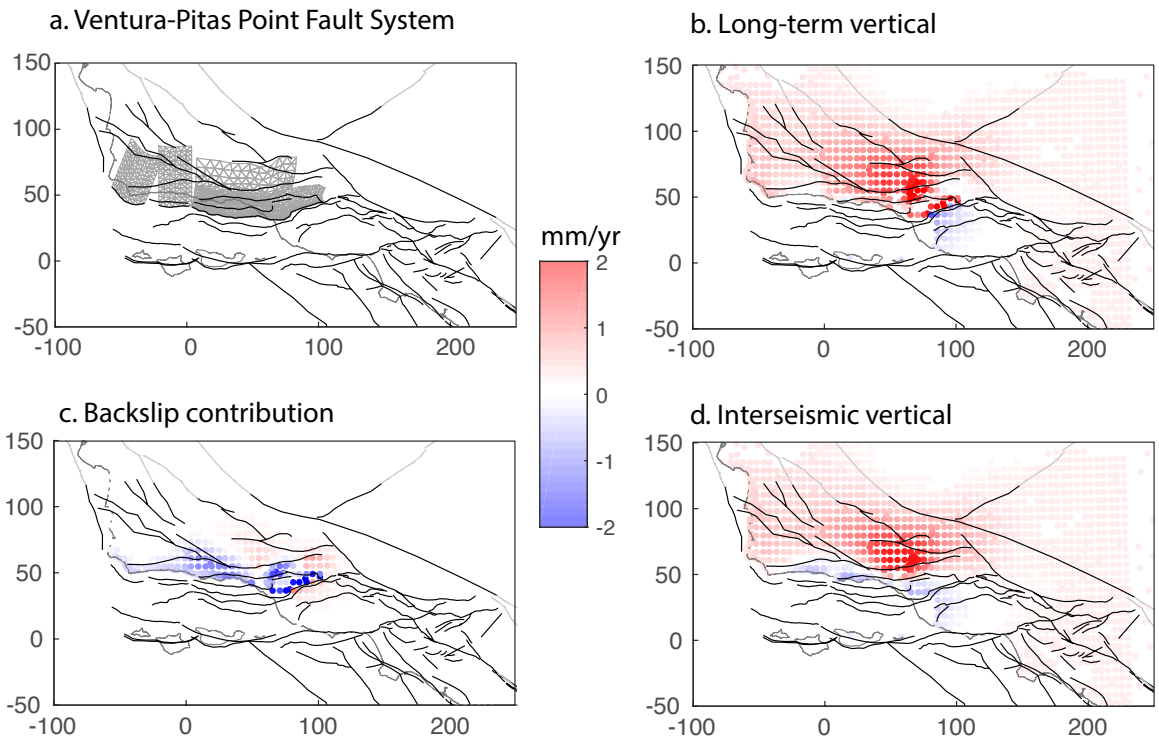

Figure 11. Contribution to vertical deformation from slip on only the Ventura-Pitas Point fault system. (a) Surface projection of Ventura-Pitas Point fault geometry. (b) Long-term vertical. (c) Vertical velocities due to backslip on locked portion of faults. (d) Interseismic vertical velocities (sum of velocities in b and c).

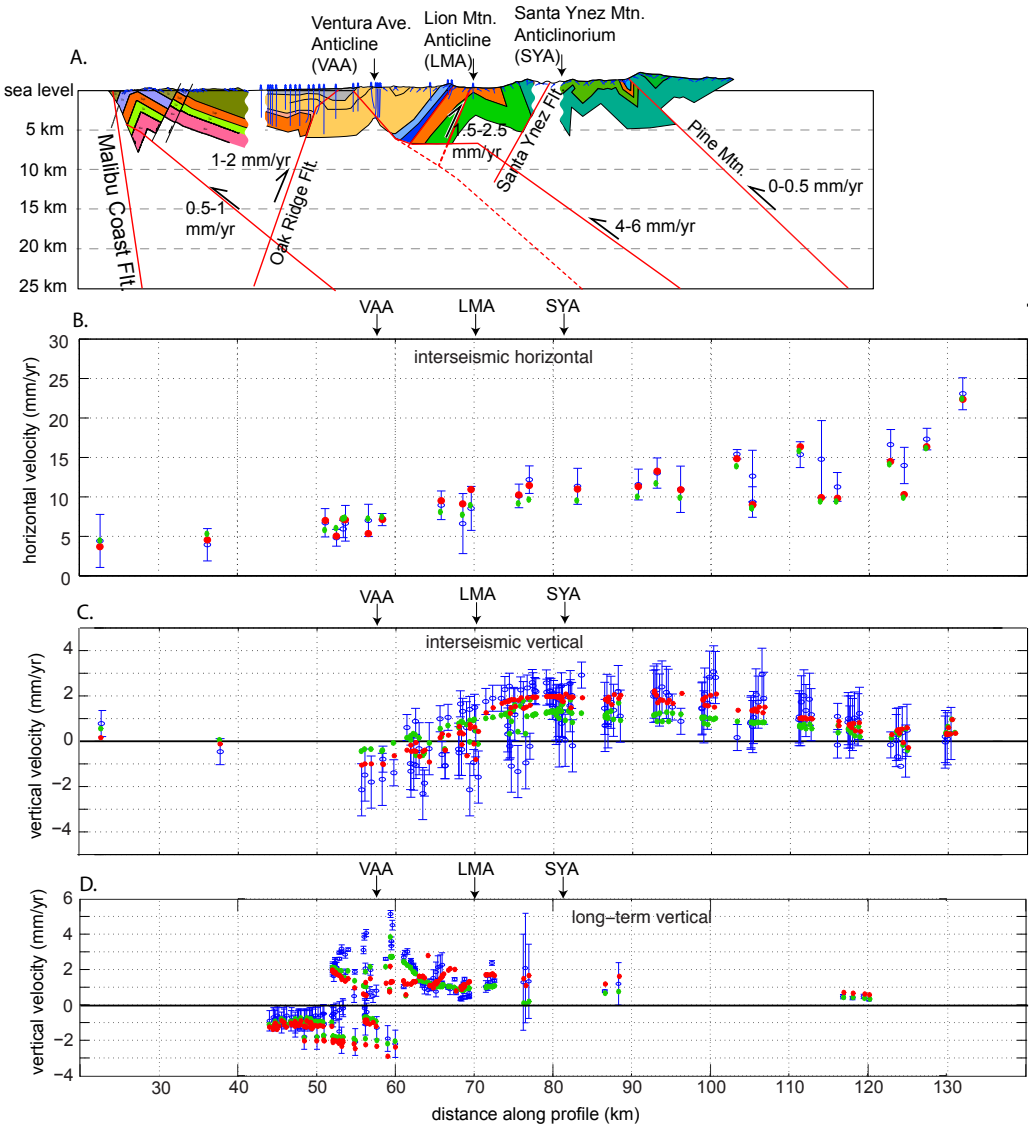

Figure 12. Compilation of geology, model, and data on cross section A-A' (location in Figure 10b). Data within 20 km of profile line are shown. (a) Shallow geology is from Namson and Davis (1988). Model faults shown with red lines along with estimated fault reverse slip rates. (b) Horizontal GPS velocities (blue error bars) and model fit (red circles for ramp-flat Ventura-Pitas Point geometry and green for straight fault geometry). Horizontal velocities are total velocities, not just component parallel to profile. (c) Same as (b) for vertical component. Broad present-day uplift across the Lion Mountain and Santa Ynez Mountain anticlinoriums is largely due to deep slip on the Ventura-Pitas Point fault system in the model. (d) Same as (b) for long-term vertical. Rapid long-term, localized uplift due to folding of the Ventura Avenue Anticline (VAA) is not captured in the model.

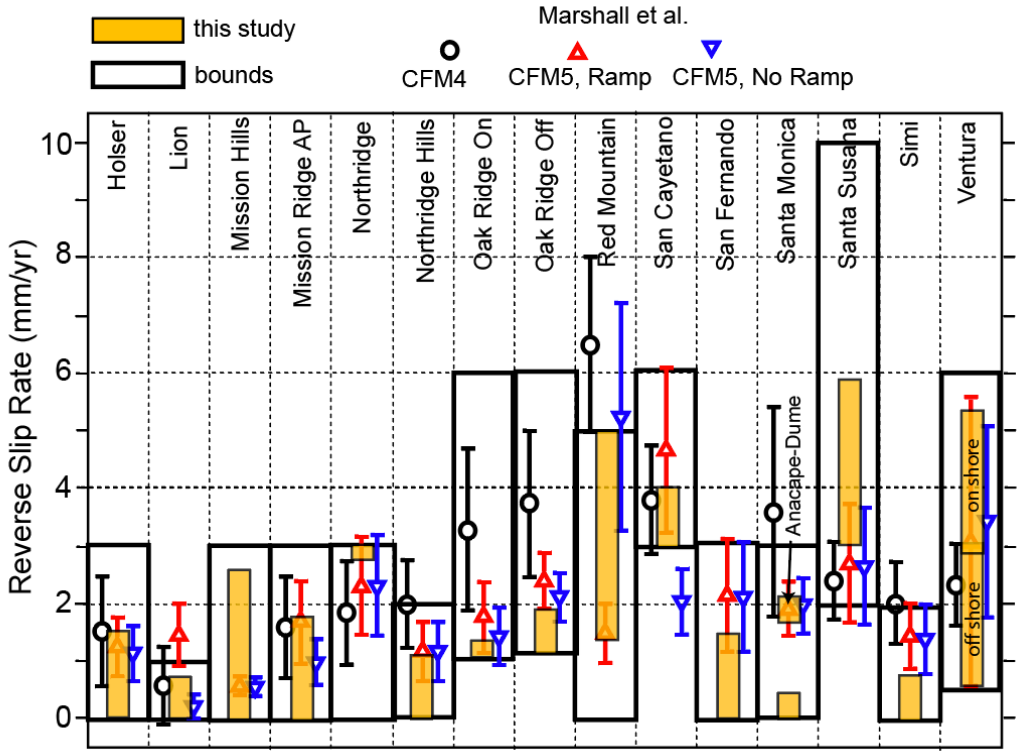

886
887 *Figure 13. Comparison of slip rate estimates from this study with assumed bounds and previous studies.*

888

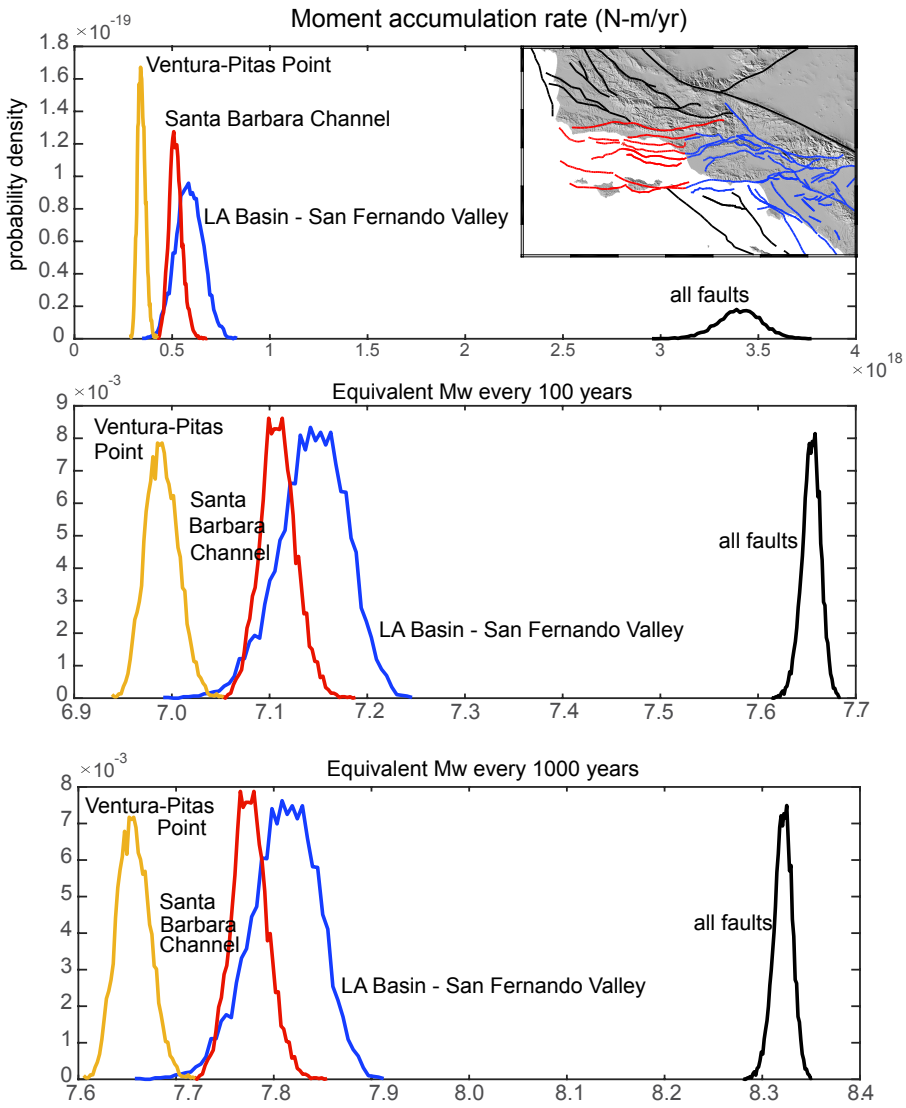

Figure 14. Computed moment accumulation rate and equivalent moment-magnitude over 100 and 1000 years on selected groups of faults. Inset shows LA Basin (blue) and Santa Barbara Channel (red) groupings.